

Pilot-wave hydrodynamics in a rotating frame: Exotic orbits

Anand U. Oza, Øistein Wind-Willassen, Daniel M. Harris, Rodolfo R. Rosales, and John W. M. Bush

Citation: [Physics of Fluids \(1994-present\)](#) **26**, 082101 (2014); doi: 10.1063/1.4891568

View online: <http://dx.doi.org/10.1063/1.4891568>

View Table of Contents: <http://scitation.aip.org/content/aip/journal/pof2/26/8?ver=pdfcov>

Published by the [AIP Publishing](#)

Articles you may be interested in

[Dynamics of a deformable active particle under shear flow](#)

J. Chem. Phys. **139**, 104906 (2013); 10.1063/1.4820416

[The pilot-wave dynamics of walking droplets](#)

Phys. Fluids **25**, 091112 (2013); 10.1063/1.4820128

[A scaling relation for the capillary-pressure driven drainage of thin films](#)

Phys. Fluids **25**, 052108 (2013); 10.1063/1.4807069

[Computational modeling of droplet based logic circuits](#)

AIP Conf. Proc. **1479**, 220 (2012); 10.1063/1.4756102

[Effects of partial miscibility on drop-wall and drop-drop interactions](#)

J. Rheol. **54**, 159 (2010); 10.1122/1.3246803



AIP | Journal of
Applied Physics

Journal of Applied Physics is pleased to
announce **André Anders** as its new Editor-in-Chief

Pilot-wave hydrodynamics in a rotating frame: Exotic orbits

Anand U. Oza,¹ Øistein Wind-Willassen,² Daniel M. Harris,¹
 Rodolfo R. Rosales,¹ and John W. M. Bush^{1,a)}

¹*Department of Mathematics, Massachusetts Institute of Technology, 77 Massachusetts Avenue, Cambridge, Massachusetts 02139, USA*

²*Department of Applied Mathematics and Computer Science, Technical University of Denmark, 2800 Kongens Lyngby, Denmark*

(Received 26 February 2014; accepted 13 July 2014; published online 1 August 2014)

We present the results of a numerical investigation of droplets walking on a rotating vibrating fluid bath. The drop's trajectory is described by an integro-differential equation, which is simulated numerically in various parameter regimes. As the forcing acceleration is progressively increased, stable circular orbits give way to wobbling orbits, which are succeeded in turn by instabilities of the orbital center characterized by steady drifting then discrete leaping. In the limit of large vibrational forcing, the walker's trajectory becomes chaotic, but its statistical behavior reflects the influence of the unstable orbital solutions. The study results in a complete regime diagram that summarizes the dependence of the walker's behavior on the system parameters. Our predictions compare favorably to the experimental observations of Harris and Bush ["Droplets walking in a rotating frame: from quantized orbits to multimodal statistics," *J. Fluid Mech.* **739**, 444–464 (2014)]. © 2014 AIP Publishing LLC. [<http://dx.doi.org/10.1063/1.4891568>]

I. INTRODUCTION

The dynamics of drops walking on the surface of a vibrating fluid bath has recently received considerable attention. As first demonstrated in Yves Couder's laboratory, these droplets exhibit several phenomena previously thought to be exclusive to the microscopic quantum realm.¹ Specifically, the walking-drop system exhibits analogs of single- and double-slit diffraction,² tunneling,³ orbital quantization,⁴ level-splitting,⁵ and wavelike statistics in confined geometries.⁶ Since the walking drop is propelled through resonant interaction with its own wave field, it represents the first macroscopic realization of a double-wave pilot-wave system, a theoretical framework for a rational quantum mechanics first envisioned by Louis de Broglie.^{7,8} We here explore the rich nonlinear dynamics that arise when a droplet walks in a rotating frame.

Consider a vertically vibrating silicone oil bath with vertical acceleration $\gamma \cos(2\pi ft)$, f being the vibrational frequency. We restrict our attention to the regime $\gamma < \gamma_F$, γ_F being the Faraday threshold,⁹ for which the fluid surface would remain flat if not for the presence of the drop. The drop generates monochromatic standing waves with decay time $T_F M_e$, M_e being the nondimensional memory parameter¹⁰

$$M_e = \frac{T_d}{T_F (1 - \gamma/\gamma_F)}, \quad (1)$$

$T_F = 2/f$ the subharmonic period and T_d the unforced decay time of the waves (arising when $\gamma = 0$), which takes a value $T_d = 0.0182$ s for 20 cS silicone oil.¹¹ Note that the memory parameter increases as the Faraday threshold is approached from below, indicating that the standing waves generated by the drop are more persistent in the high-memory limit, as arises when $\gamma \rightarrow \gamma_F$.

^{a)}Electronic mail: bush@math.mit.edu

Protière, Boudaoud, and Couder¹² demonstrated that millimetric drops may move horizontally, or walk, across the vibrating fluid surface while bouncing vertically. A comprehensive theoretical and experimental study of the walker dynamics was conducted by Moláček and Bush^{11,13} and Wind-Willassen *et al.*,¹⁴ who rationalized the various bouncing and walking states. Specifically, their analysis produced a series of regime diagrams rationalizing the observed dependence of the drop's dynamical behavior on the system parameters.¹²

Oza, Rosales, and Bush¹⁵ built upon the model of Moláček and Bush¹¹ to develop an integro-differential equation describing the horizontal motion of a “resonant walker,” a droplet bouncing periodically at frequency $f/2$, synchronized with its wave field. The resulting trajectory equation captured several key features of the walker dynamics, including the supercritical pitchfork bifurcation to walking, the dependence of the walking speed on the vibrational forcing, and the stability of the walking state.

Fort *et al.*⁴ conducted the first investigation of the walker dynamics in a rotating frame. When placed in a fluid bath rotating about its centerline with angular frequency $\Omega = \Omega \hat{z}$, a walker of mass m and speed u_0 executes circular orbits in the rotating frame of reference. The authors report that the orbital radius depends on the memory. At low memory, the dominant force balance is between the walker's inertial force mu_0^2/r_c and the Coriolis force $2m\Omega u_0$, which results in a circular orbit of radius $r_c \approx u_0/2\Omega$. At high memory, the orbital radius no longer decreases continuously with the rotation rate, and the orbital radii become quantized. Bands of forbidden orbital radii emerge with increasing memory, and multiple orbital solutions may coexist for a given rotation rate Ω . Based on the analogous forms of the Coriolis force $\mathbf{F} = 2m\dot{\mathbf{x}} \times \boldsymbol{\Omega}$ acting on a mass m in a rotating frame and the Lorentz force $\mathbf{F} = q\dot{\mathbf{x}} \times \mathbf{B}$ acting on a charge q in the presence of a magnetic field \mathbf{B} , the authors⁴ propose an analogy between the walker's quantized orbits and the Landau levels of an electron. Their accompanying theoretical model rationalized the quantized orbits as resulting from a memory effect.

Harris and Bush¹⁶ conducted a comprehensive experimental study of the same system, which revealed a number of new phenomena. At high memory, in addition to quantized orbits, the authors report the existence of wobbling orbits, marked by a periodic fluctuation in the orbital radius. They also observe drifting orbits, in which the orbital center of a wobbling orbit traverses a nearly circular path. At higher values of memory, they report wobble-and-leap dynamics, in which the trajectory of the orbital center is characterized by a slow drift punctuated by short bursts of rapid motion. At the highest memory considered, they report that the walker's trajectory becomes erratic, presumably chaotic. Nevertheless, the histogram of its radius of curvature has a coherent multimodal structure, with peaks arising at the radii of the unstable quantized circular orbits.

The observed orbital quantization was rationalized theoretically through a linear stability analysis of circular orbits,^{17,18} which is summarized in Fig. 1. Each point on the diagram corresponds to a particular orbital radius r_0 and vibrational forcing γ . Orbits indicated in red are unstable so were not observed experimentally. Stable orbits, indicated in blue, thus become quantized at high memory. These quantized orbits are labeled by n , $n = 0$ being the smallest, and larger n corresponding to larger orbits. Other orbits, indicated in green, destabilize via an oscillatory mechanism, which can give rise to wobbling orbits in the laboratory.¹⁶ The analysis also predicts the relative absence of stable circular orbits in the high-memory limit, $\gamma \rightarrow \gamma_F$. Note, however, that the linear stability analysis can only assess the stability of the circular orbits and cannot provide insight into the dynamics arising within the unstable regions. Such nonlinear dynamics is the subject of this paper.

Through numerical simulation of a single walker in a rotating frame, we characterize its behavior as a function of the forcing acceleration γ and rotation rate Ω . In addition to reproducing many of the experimental results of Harris and Bush,¹⁶ we report a number of new states marked by complex periodic and quasiperiodic trajectories. Our study culminates in a complete regime diagram indicating the dependence of the walker's behavior on the system parameters.

In Sec. II, we review the hydrodynamic trajectory equation¹⁷ for walking drops in a rotating frame and explain the numerical method used to simulate the walker dynamics. We describe wobbling orbits in Sec. III, drifting orbits in Sec. IV, and wobble-and-leap dynamics in Sec. V. Other complex periodic and quasiperiodic trajectories are described in Sec. VI, and the statistical behavior of chaotic trajectories is discussed in Sec. VII. Future directions are discussed in Sec. VIII.

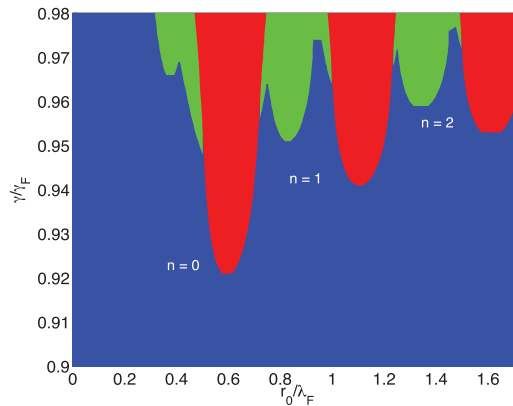


FIG. 1. Summary of the linear stability analysis for circular orbits,^{17,18} for a walker of radius 0.4 mm bouncing on a 20 cS silicone oil bath forced at 80 Hz. The dimensionless orbital radius r_0/λ_F and vibrational acceleration γ/γ_F uniquely specify the circular orbit. Blue indicates stable orbits, for which each eigenvalue has a negative real part. Green corresponds to unstable orbits with an oscillatory instability, for which the eigenvalues with the largest (positive) real part are complex conjugates. Red corresponds to unstable orbits for which the eigenvalue with the largest (positive) real part is purely real.

II. TRAJECTORY EQUATION AND NUMERICAL METHOD

We first review the trajectory equation for a resonant walker in a rotating frame, the complete derivation of which has been presented elsewhere.¹⁷ Let $\mathbf{x}(t) = (x(t), y(t))$ denote the horizontal position of the walker at time t . The horizontal force balance on the walker, time-averaged over the bouncing period, yields the following integro-differential equation of motion:^{15,17}

$$m\ddot{\mathbf{x}} + D\dot{\mathbf{x}} = \frac{F}{T_F} \int_{-\infty}^t \frac{J_1(k_F |\mathbf{x}(t) - \mathbf{x}(s)|)}{|\mathbf{x}(t) - \mathbf{x}(s)|} (\mathbf{x}(t) - \mathbf{x}(s)) e^{-(t-s)/(T_F M_e)} ds - 2m\boldsymbol{\Omega} \times \dot{\mathbf{x}}. \quad (2)$$

The walker moves in response to three forces: a drag force $-D\dot{\mathbf{x}}$, the Coriolis force $-2m\boldsymbol{\Omega} \times \dot{\mathbf{x}}$, and a propulsive wave force proportional to the local slope of the fluid interface. During each impact, the walker generates a monochromatic standing wave with spatial profile $J_0(k_F r)$, frequency $f/2$ and decay time $T_F M_e$, where the Faraday wavelength $\lambda_F = 2\pi/k_F$ approximately satisfies the water-wave dispersion relation¹⁹ $(\pi f)^2 = (gk_F + \sigma k_F^3/\rho) \tanh k_F H$. Formulae for the time-averaged drag coefficient D and wave force coefficient F in terms of the fluid parameters were derived by Moláček and Bush¹¹ and are listed in Table I. There are no free parameters in this model. The simulations in this study were performed using the fluid parameters approximately corresponding to the silicone oil used in the experiments of Harris and Bush,¹⁶ with $\rho = 949 \text{ kg/m}^3$, $\nu = 20 \text{ cS}$, $\sigma = 0.206 \text{ N/m}$, $H = 4 \text{ mm}$, $f = 80 \text{ Hz}$, $R_D = 0.4 \text{ mm}$, and $\sin \Phi = 0.2$.

We non-dimensionalize (2) by introducing dimensionless variables $\hat{\mathbf{x}} = k_F \mathbf{x}$, $\hat{t} = t/T_F M_e$, and $\hat{\boldsymbol{\Omega}} = 2m\boldsymbol{\Omega}/D$. Using primes to denote differentiation with respect to \hat{t} , the trajectory equation becomes

$$\kappa \hat{\mathbf{x}}'' + \hat{\mathbf{x}}' = \beta \int_{-\infty}^{\hat{t}} \frac{J_1(|\hat{\mathbf{x}}(\hat{t}) - \hat{\mathbf{x}}(\hat{s})|)}{|\hat{\mathbf{x}}(\hat{t}) - \hat{\mathbf{x}}(\hat{s})|} (\hat{\mathbf{x}}(\hat{t}) - \hat{\mathbf{x}}(\hat{s})) e^{-(\hat{t}-\hat{s})} d\hat{s} - \hat{\boldsymbol{\Omega}} \times \hat{\mathbf{x}}', \quad (3)$$

where $\kappa = m/DT_F M_e$ and $\beta = Fk_F T_F M_e^2/D$.

We proceed by outlining the procedure used to numerically simulate the walker's trajectory. We assume the walker to be in a circular orbit prior to the initial time $t = 0$, that is, $\hat{\mathbf{x}}(t) = \hat{\mathbf{x}}_O(t) = (\hat{r}_0 \cos \hat{\omega} \hat{t}, \hat{r}_0 \sin \hat{\omega} \hat{t})$ for $t < 0$, where \hat{r}_0 and $\hat{\omega}$ are defined in terms of M_e and $\hat{\boldsymbol{\Omega}}$ through the following equations:¹⁷

$$\begin{aligned} -\kappa \hat{r}_0 \hat{\omega}^2 &= \beta \int_0^\infty J_1 \left(2\hat{r}_0 \sin \frac{\hat{\omega} z}{2} \right) \sin \frac{\hat{\omega} z}{2} e^{-z} dz + \hat{\boldsymbol{\Omega}} \hat{r}_0 \hat{\omega} \\ \hat{r}_0 \hat{\omega} &= \beta \int_0^\infty J_1 \left(2\hat{r}_0 \sin \frac{\hat{\omega} z}{2} \right) \cos \frac{\hat{\omega} z}{2} e^{-z} dz. \end{aligned} \quad (4)$$

TABLE I. The variables appearing in the trajectory equations (2) and (3).

Dimensional variables	Definition
m	Drop mass
R_D	Drop radius
ν	Fluid kinematic viscosity
σ	Fluid surface tension
ρ	Fluid density
μ_a	Air dynamic viscosity
ρ_a	Air density
f	Forcing frequency
γ	Forcing acceleration
γ_F	Faraday instability threshold
g	Gravitational acceleration
$T_F = 2/f$	Faraday period
T_d	Decay time of waves without forcing
$k_F = 2\pi/\lambda_F$	Faraday wavenumber, wavelength
Φ	Mean phase of wave during contact
$D = 0.17mg\sqrt{\frac{\rho R_D}{\sigma}} + 6\pi\mu_a R_D \left(1 + \frac{\rho_a g R_D}{12\mu_a f}\right)$	Drag coefficient
$F = \sqrt{\frac{1.5795\nu}{2\pi T_F}} \frac{mgk_F^4}{3k_F^2\sigma + \rho g} mg T_F \sin \Phi$	Wave force coefficient
$\Omega = \Omega \hat{z}$	Angular frequency of bath
Nondimensional variables	
$M_e = \frac{T_d}{T_F(1-\gamma/\gamma_F)}$	Memory
$\kappa = \frac{m}{DT_F M_e}$	Nondimensional mass
$\beta = \frac{Fk_F T_F M_e^2}{D}$	Nondimensional wave force coefficient
$\hat{\Omega} = \frac{2m\Omega}{D}$	Nondimensional angular frequency of bath

The walker's trajectory is evolved in time using the fourth-order Adams-Bashforth linear multistep method.²⁰ Dropping the hats, the numerical scheme may be written as

$$\begin{aligned}
 \mathbf{x}_{n+1} &= \mathbf{x}_n + \Delta t \sum_{m=0}^3 c_m \mathbf{u}_{n-m} \\
 \mathbf{u}_{n+1} &= \mathbf{u}_n + \frac{\Delta t}{\kappa} \sum_{m=0}^3 c_m \left[-\mathbf{u}_{n-m} - \Omega \times \mathbf{u}_{n-m} + \beta f_0(\mathbf{x}_{n-m}) e^{-t_{n-m}} \right. \\
 &\quad \left. + \beta \int_0^{t_{n-m}} \frac{J_1(|\mathbf{x}_{n-m} - \mathbf{x}(s)|)}{|\mathbf{x}_{n-m} - \mathbf{x}(s)|} (\mathbf{x}_{n-m} - \mathbf{x}(s)) e^{-(t_{n-m}-s)} ds \right] \\
 f_0(\mathbf{x}) &= \int_{-\infty}^0 \frac{J_1(|\mathbf{x} - \mathbf{x}_O(s)|)}{|\mathbf{x} - \mathbf{x}_O(s)|} (\mathbf{x} - \mathbf{x}_O(s)) e^s ds,
 \end{aligned} \tag{5}$$

where Δt is the time step, $t_n = n\Delta t$, $\mathbf{x}_n = \mathbf{x}(t_n)$, and $\mathbf{u}_n = \mathbf{u}(t_n)$. The coefficients are²⁰ $c_0 = 55/24$, $c_1 = -59/24$, $c_2 = 37/24$, and $c_3 = -3/8$. The integral in (5) is computed using Simpson's rule, and $f_0(\mathbf{x})$ using an adaptive Gauss-Kronrod quadrature routine built into MATLAB. The first four time steps ($n = 0, 1, 2, 3$) employ the assumption that $\mathbf{x} = \mathbf{x}_O$ for $t < 0$, so $\mathbf{x}_j = \mathbf{x}_O(t_j)$ and $\mathbf{u}_j = \dot{\mathbf{x}}_O(t_j)$ for $j < 0$. Unless otherwise stated, the simulations in this study were performed with a fixed time step $\Delta t = 2^{-6}$ and initial perturbation $\delta = (0.02, 0)$, so that $\mathbf{x}_0 = \mathbf{x}_O(0) + \delta$. The trajectory was evolved beyond $t_{\max} = 1000$, typically a sufficiently large value to capture its asymptotic behavior.

We proceed by characterizing the dependence of the walker's trajectory on its initial orbital radius r_0 and forcing acceleration γ/γ_F , with a resolution $\Delta(\gamma/\gamma_F) = 0.001$. The resulting dynamics is classified in Fig. 2, where each color corresponds to a different type of trajectory. Once again, blue denotes regions in which the circular orbit is stable. Pink and red denote jumping orbits, for which

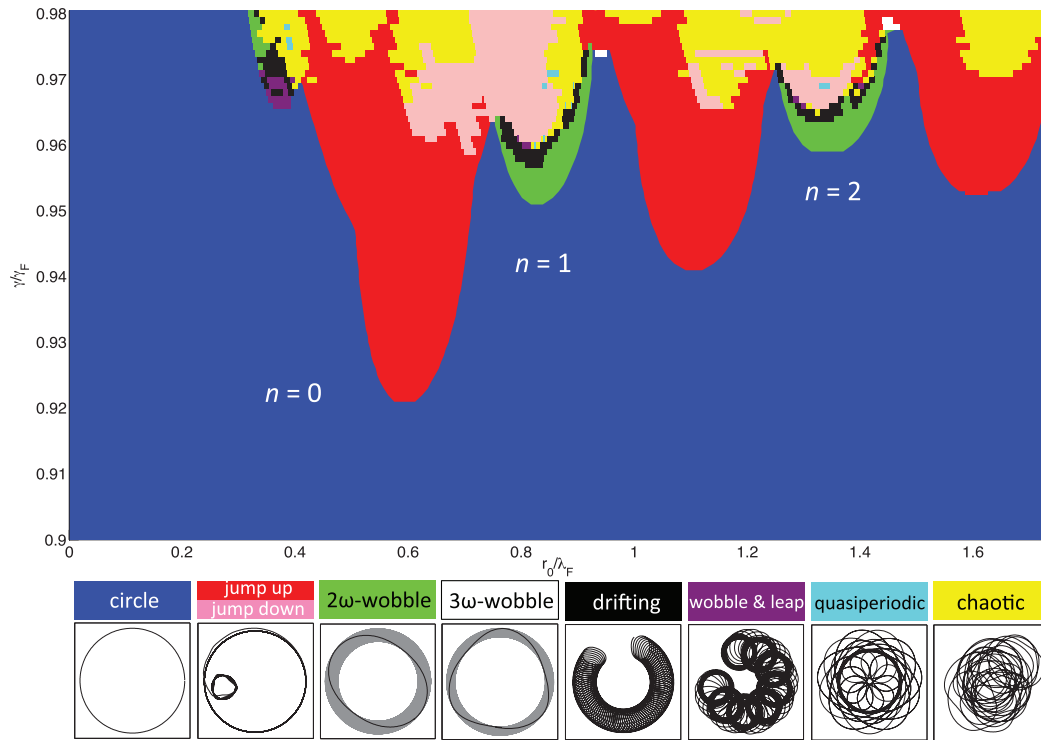


FIG. 2. Regime diagram delineating the dependence of the walker's trajectory on the initial orbital radius r_0 and vibrational forcing γ . The trajectory equation (3) is numerically simulated using circular orbit initial conditions, initial perturbation $\delta = (0.02, 0)$, time step $\Delta t = 2^{-6}$, and $t_{max} = 1000$. The walker's trajectory is color-coded according to the legend.

the initial circular orbit destabilizes into a different circular orbit, or into a quasiperiodic orbit with a significantly different mean radius. Those in pink jump to a trajectory with a smaller mean radius, and those in red jump to larger orbits. Green and white denote 2ω - and 3ω -wobbling orbits, which are respectively characterized by a radial oscillation with approximately twice and thrice the orbital frequency. Black denotes drifting orbits, and purple denotes wobble-and-leap orbits. The orbits in light blue correspond to other complex periodic or quasiperiodic orbits. The yellow regions denote erratic or chaotic trajectories for which there is no discernible periodic pattern. We note that the linear stability boundary for circular orbits, as indicated in Fig. 1, does not conclusively determine the walker's nonlinear behavior. For example, the green boundaries in the vicinity of $\gamma/\gamma_F = 0.955$ in Fig. 1 indicate an oscillatory instability of circular orbits, but correspond to wobbling or jumping orbits.

For the initial orbital radii explored, $0 < r_0/\lambda_F < 1.73$, all circular orbits are stable for $\gamma/\gamma_F \leq 0.921$, and only jumping or erratic orbits are present for $\gamma/\gamma_F > 0.98$ and $r_0/\lambda_F > 0.32$. In Secs. III–VII, we detail the various trajectories observed.

III. WOBBLING ORBITS

We here report two different types of wobbling orbits found in our numerical explorations. The existence of 2ω -wobbling orbits, indicated by the green regions in Fig. 2, was suggested theoretically by the linear stability analysis of circular orbits^{17,18} and has been reported in laboratory experiments.¹⁶ Figure 3(a) shows a typical wobbling orbit at $n = 1$, which has a slightly oblong shape. Let \bar{x}_c be the stationary orbital center, defined as the mean value of $x(t)$ over the entire trajectory. The orbital radius $\bar{r}(t) = |x(t) - \bar{x}_c|$ is plotted in Fig. 3(b). The top panel shows that the circular orbit solution with constant radius $r_0/\lambda_F = 0.85$ becomes unstable in an oscillatory fashion, and that the radial oscillations saturate after a finite time, which is characteristic of a Hopf-type instability. A small portion of the time trace of $\bar{r}(t)$, displayed in the lower panel, confirms that the

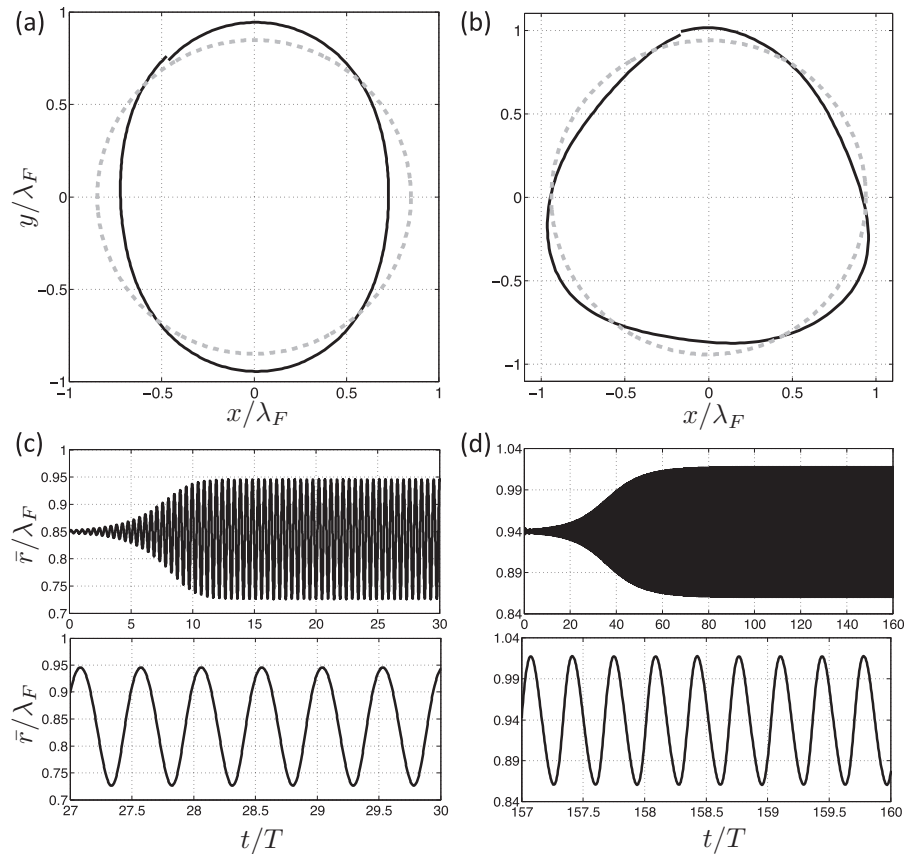


FIG. 3. Panels (a) and (b): examples of 2ω - and 3ω -wobbling orbits at $n = 1$, respectively. The 2ω -wobbling orbit was obtained using initial orbital radius $r_0/\lambda_F = 0.85$ and vibrational forcing $\gamma/\gamma_F = 0.955$, and the 3ω -wobbling orbit using $r_0/\lambda_F = 0.94$ and $\gamma/\gamma_F = 0.9745$. The corresponding (unstable) circular orbit is indicated by the dashed line. Panels (c) and (d): plots of the corresponding orbital radius $\bar{r}(t)$ as a function of t/T , where T is the orbital period. In the upper plots, note that the radius grows and then saturates, which is characteristic of a Hopf-type instability. The lower plots resolve the oscillations, showing that the wobbling frequency is $\approx 2\omega$ in (c) and $\approx 3\omega$ in (d).

wobbling frequency is roughly twice the orbital frequency. The orbital period T is obtained by taking the Fourier transform of the trajectory $\mathbf{x}(t)$ and identifying the dominant frequency.

An example of a roughly triangular 3ω -wobbling orbit, indicated by the white regions in Fig. 2, is shown in Fig. 3(c). The lower panel of Fig. 3(d) shows that the wobbling frequency of $\bar{r}(t)$ is roughly thrice the orbital frequency. These 3ω -wobbling orbits have not yet been found in laboratory experiments, presumably because they arise only in a minuscule region of parameter space.

We further characterize the 2ω -wobbling orbits by comparing their wobbling amplitudes and frequencies to those observed in the laboratory experiments of Harris and Bush.¹⁶ The wobbling frequency ω_{wob} is obtained by taking the Fourier transform of the signal $\bar{r}(t)$ and identifying the largest peak. The wobbling amplitude A is then defined as

$$A = \sqrt{2} \left[\frac{1}{T_{\text{wob}}} \int_{T_{\text{wob}}} (\bar{r}(t) - \bar{r}_a)^2 dt \right]^{1/2}, \quad \text{where } \bar{r}_a = \frac{1}{T_{\text{wob}}} \int_{T_{\text{wob}}} \bar{r}(t) dt \quad (6)$$

is the mean orbital radius and $T_{\text{wob}} = 2\pi/\omega_{\text{wob}}$ the wobbling period. Figure 4(a) shows the dependence of the wobbling amplitude A on the rotation rate Ω for various values of the forcing acceleration γ/γ_F . The breaks in the curves correspond to regions in which wobbling orbits are absent, a feature that will be discussed in Sec. IV.

We note a number of features that are consistent with the corresponding experimental observations of Harris and Bush,¹⁶ as are reproduced in Fig. 4(b). The qualitative shape of the experimental

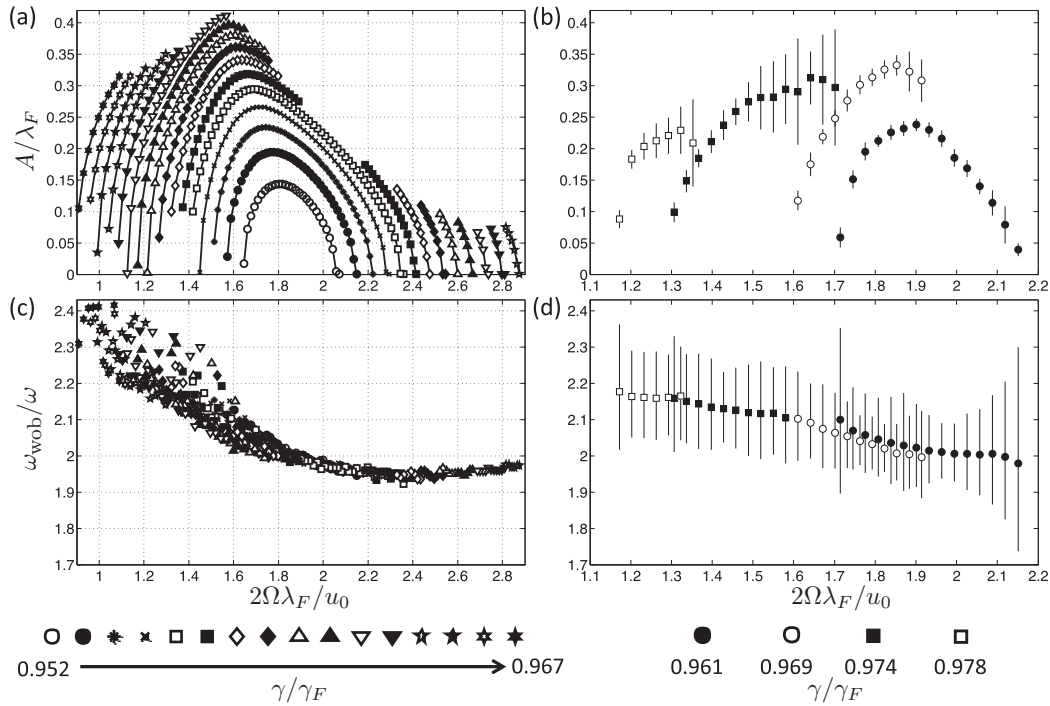


FIG. 4. Numerical characterization of wobbling orbits (panels (a) and (c)), compared with experimental data from Harris and Bush¹⁶ (panels (b) and (d)). Panels (a) and (b) show the dependence of the wobbling amplitude A on the rotation rate Ω for various values of memory γ/γ_F . Panels (c) and (d) show the dependence of the wobbling frequency ω_{wob} on the rotation rate Ω . The wobbling frequency is normalized by the orbital frequency ω . The symbols correspond to different values of the memory γ/γ_F , as defined in the legend.

curve at $\gamma/\gamma_F = 0.961$ is similar to the numerically generated curves at the lowest memory, $\gamma/\gamma_F = 0.952$ to 0.956 . At higher values of memory, the experimental curves ($\gamma/\gamma_F \geq 0.969$) and numerical curves ($\gamma/\gamma_F \geq 0.965$) end abruptly, indicating that the wobbling amplitude does not decrease smoothly to zero with increasing rotation rate. The onset of wobbling occurs for lower values of Ω as memory is increased, and the wobbling amplitude increases with memory for a fixed value of Ω . Note that the wobbling amplitudes obtained in the numerical simulations are roughly consistent with experiment. However, the data points do not coincide precisely, presumably because the system is highly sensitive to small deviations in drop size and fluid viscosity. Nevertheless, it is clear that our model results capture the essential dynamical features of the observed wobbling orbits.

The dependence of the wobbling frequency ω_{wob} on the rotation rate Ω is shown in Fig. 4(c), which is qualitatively consistent with the experimental data¹⁶ reproduced in Fig. 4(d). Note that the wobbling frequencies for a wide range of memory values lie near a single curve, an effect that can be rationalized through the linear stability analysis of circular orbits.¹⁸ The wobbling frequency typically decreases slowly with rotation rate while remaining close to the value 2ω .

IV. DRIFTING ORBITS

At higher values of memory, wobbling orbits destabilize, their orbital centers drifting in a regular fashion on a timescale long relative to the orbital period. Drifting orbits are denoted by the black regions in Fig. 2. We define the orbital center $\bar{\mathbf{x}}_c(t)$ of a drifting orbit as the average value of $\mathbf{x}(t)$ over an orbital period T ,

$$\bar{\mathbf{x}}_c(t) = \frac{1}{T} \int_t^{t+T} \mathbf{x}(s) ds. \quad (7)$$

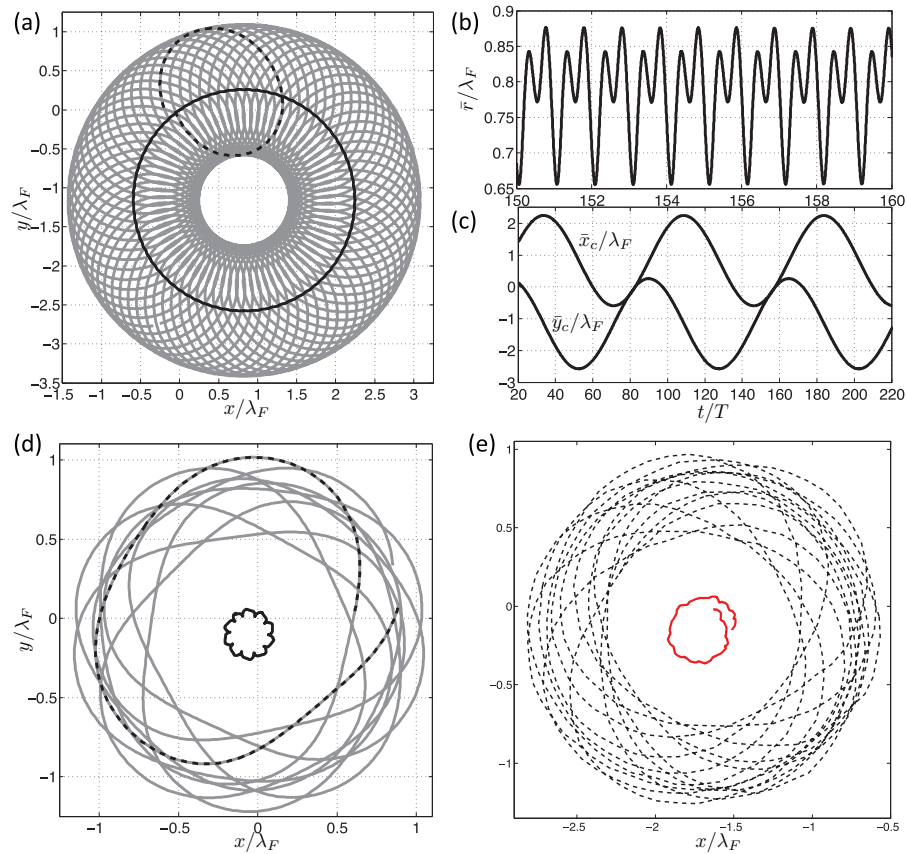


FIG. 5. (a) Numerical simulation of a drifting trajectory at $n = 1$, obtained using the initial orbital radius $r_0/\lambda_F = 0.8005$ and vibrational forcing $\gamma/\gamma_F = 0.959$. The trajectory (gray line) consists of a loop (dashed line) drifting along a larger circle (black solid line). (b) Plot of the orbital radius $\bar{r}(t)$ as a function of t/T , where $T = 4.3$ is the orbital period. (c) Plot of the orbital center (\bar{x}_c, \bar{y}_c) as a function of t/T . Note that the center moves on a much slower timescale than the radius \bar{r} . (d) Numerical simulation of another drifting trajectory using $r_0/\lambda_F = 0.893$ and $\gamma/\gamma_F = 0.966$, for which the center does not move along a precise circle. (e) Experimentally observed¹⁶ drifting trajectory similar to that in panel (d), obtained using $\gamma/\gamma_F = 0.978 \pm 0.003$ and rotation rate $\Omega = 1.72 \text{ s}^{-1}$. The trajectory is indicated by the dashed line, the motion of the center by the solid line.

An example of a drifting orbit is shown in Fig. 5. The time trace of the orbital radius $\bar{r}(t) = |\mathbf{x}(t) - \bar{\mathbf{x}}_c(t)|$ suggests that the drifting orbit arises from the period-doubling bifurcation of a wobbling orbit, a phenomenon to be detailed elsewhere. Note that the period of the orbital center is much larger than the orbital period T , this slow oscillation being characteristic of drifting orbits. Figure 5(d) shows another example of a drifting orbit, alongside its experimental counterpart as reported by Harris and Bush¹⁶ (Fig. 5(e)).

In Figs. 6(a) and 6(d), we illustrate the relationship between circular, wobbling, and drifting orbits at the second orbital, $n = 1$, for two particular values of memory, $\gamma/\gamma_F = 0.957$ and 0.958 . Stable circular orbits are indicated by the blue curve, and unstable ones by the green curve. The mean radii \bar{r}_a of the wobbling orbits, which lie on the green curve, are marked by the data points, the error bars reflecting the wobbling amplitude A . The wobbling orbits destabilize into drifting orbits in the open green regions of the two curves, which are reflected by the breaks in the corresponding wobbling amplitude curves in Fig. 4(a). For these values of memory, the orbital center $\bar{\mathbf{x}}_c(t)$ of a drifting orbit is found to traverse a circular path of radius R_{drift} over a period T_{drift} . Figures 6(b) and 6(e) show that the drift radius R_{drift} depends continuously on the rotation rate Ω for these two values of memory. Unlike the wobbling frequency (Fig. 4(c)), the drift period T_{drift} exhibits a strong dependence on the rotation rate, as shown in Figs. 6(c) and 6(f). The large values of T_{drift}/T indicate that drifting orbits evolve over a timescale long relative to the orbital period, making experimental exploration of the

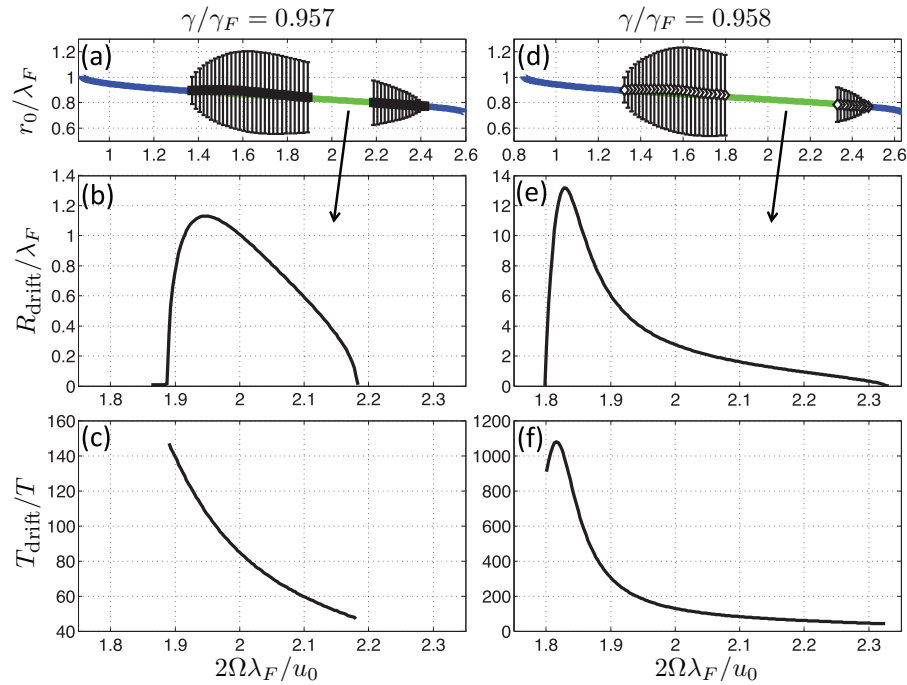


FIG. 6. Numerical characterization of drifting orbits at $n = 1$. Top panels (a) and (d): the curve shows the theoretical orbital radius r_0 as a function of the nondimensional rotation rate $2\Omega\lambda_F/u_0$, calculated using (4). The blue segments indicate stable circular orbits, and the green unstable solutions due to an oscillatory instability. The trajectory equation (3) was numerically simulated within the green regions, and both wobbling and drifting orbits were found. The markers correspond to the mean orbital radius \bar{r} of a wobbling orbit, and the error bars indicate the wobbling amplitude. The unmarked green regions correspond to drifting orbits, in which the orbital center (\bar{x}_c, \bar{y}_c) drifts in a circle. The middle panels, (b) and (e), show the radius R_{drift} of the orbital center, and the lower panels (c) and (f) the period of the orbital center T_{drift} normalized by the orbital period T . Panels (a)–(c) correspond to a vibrational forcing $\gamma/\gamma_F = 0.957$ and (d)–(f) to $\gamma/\gamma_F = 0.958$.

curves in Fig. 6 impractical. For higher values of memory, $\gamma/\gamma_F \geq 0.959$, the orbital centers $\bar{x}_c(t)$ of some drifting orbits follow irregular noncircular paths, indicating that simple drifting orbits may destabilize into more complex trajectories. We expect qualitatively similar behavior to arise at the higher orbital levels, $n > 1$.

An example of a drifting orbit at the innermost orbital level, $n = 0$, is shown in Fig. 7(a). Such orbits were found in the black portions of the $n = 0$ region in Fig. 2. The walker's trajectory (gray curve) consists of a loop (dashed black curve) that drifts along a square epicycle (black

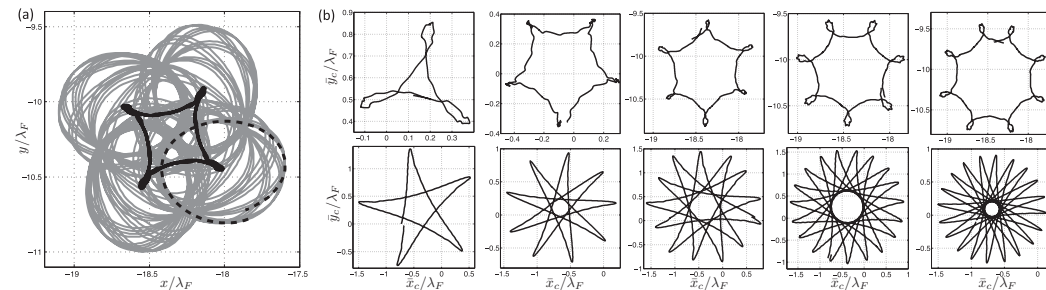


FIG. 7. Numerical simulations of drifting orbits, for various values of the vibrational forcing γ/γ_F and initial orbital radius r_0 . In panel (a), the gray curve corresponds to a trajectory with $r_0/\lambda_F = 0.7262$ and $\gamma/\gamma_F = 0.971$, which consists of a loop (dashed black curve) that drifts along a square epicycle (black curve). The plots along the top row of panel (b) show the orbital centers of some drifting orbits at $n = 0$. From left to right, the parameter values are: $(r_0/\lambda_F, \gamma/\gamma_F) = (0.7221, 0.973)$, $(0.3635, 0.968)$, $(0.7514, 0.971)$, $(0.7870, 0.971)$, and $(0.775, 0.971)$. The bottom row shows those corresponding to $n = 1$, with parameter values $(r_0/\lambda_F, \gamma/\gamma_F) = (0.8541, 0.9612)$, $(0.8537, 0.9609)$, $(0.8541, 0.96125)$, $(0.8542, 0.9613)$, and $(0.8537, 0.96085)$, which correspond to the same dimensionless rotation rate $\hat{\Omega} = 0.5734$.

curve). As the rotation rate Ω and memory are slightly varied, the orbital center $\bar{\mathbf{x}}_c(t)$ is found to drift along a variety of epicycoidal paths, as shown in the top row of Fig. 7(b). The orbital center associated with an $n = 1$ orbit may traverse a star-shaped path, as shown in the bottom row of Fig. 7(b). However, such regular drifting orbits arise in a relatively narrow range of parameter space, outside of which the orbital centers drift with a relatively incoherent pattern.

V. WOBBLE-AND-LEAP DYNAMICS

The purple regions in Fig. 2 denote wobble-and-leap trajectories, which are characterized by a sequence of alternating wobbling and leaping phases.¹⁶ During the wobbling phase, the orbital radius grows in an oscillatory fashion, while the orbital center remains stationary. The orbital center then rapidly jumps to a new location, after which the process begins anew.

Wobble-and-leap trajectories at $n = 1$ appear to arise from the instability of the drifting orbits in response to increased memory. A numerical example of such a trajectory is given in Fig. 8. The orbital center $\bar{\mathbf{x}}_c(t)$ (panels (c) and (d)) remains relatively stationary while the oscillations in the

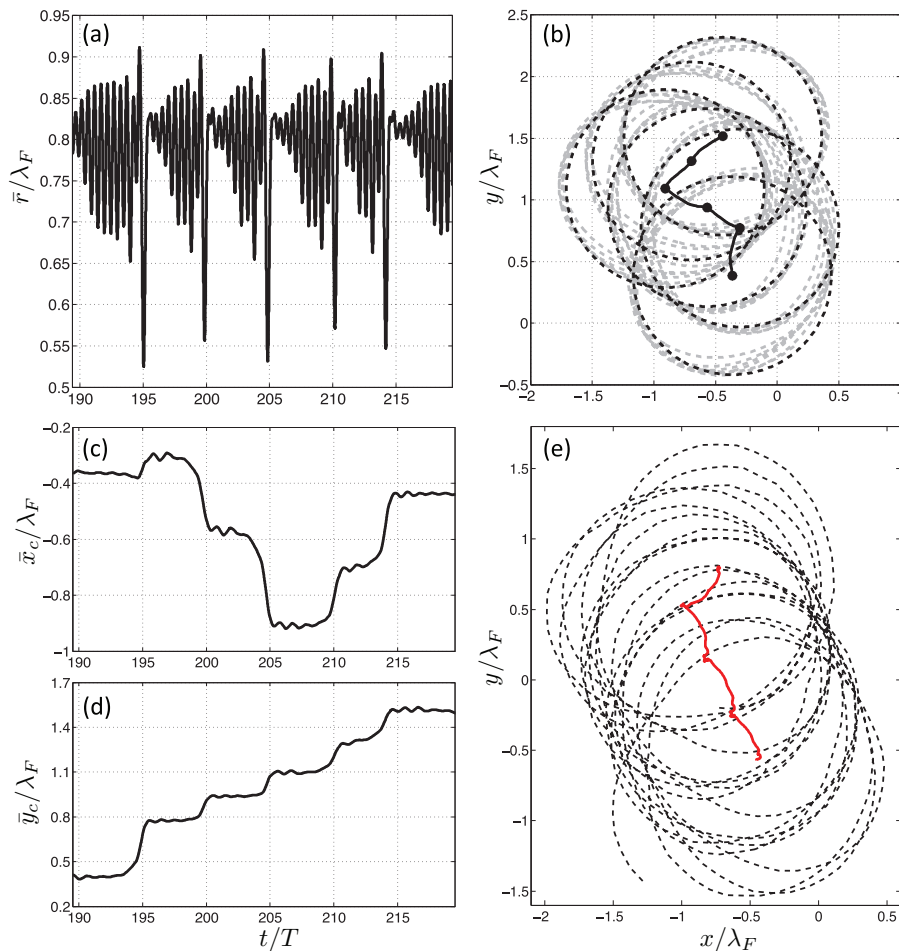


FIG. 8. Numerical simulation of a wobble-and-leap trajectory at $n = 1$, obtained using initial orbital radius $r_0/\lambda_F = 0.8029$ and vibrational forcing $\gamma/\gamma_F = 0.960$. Panel (a) shows the mean orbital radius $\bar{r}(t)$. Panel (b) shows the trajectory (dashed gray curve), resulting from the orbital center (solid black curve) jumping between the transiently stable points (black dots). The dashed black curves are circles of radius r_0/λ_F centered on the stable points. Panels (c) and (d) show the coordinates $\bar{x}_c(t)$ and $\bar{y}_c(t)$ of the orbital center. Panel (e) shows a qualitatively similar trajectory observed in the experiments of Harris and Bush,¹⁶ obtained using $\gamma/\gamma_F = 0.978 \pm 0.003$ and rotation rate $\Omega = 1.76 \text{ s}^{-1}$. The trajectory is indicated by the dashed line, the center by the solid line.

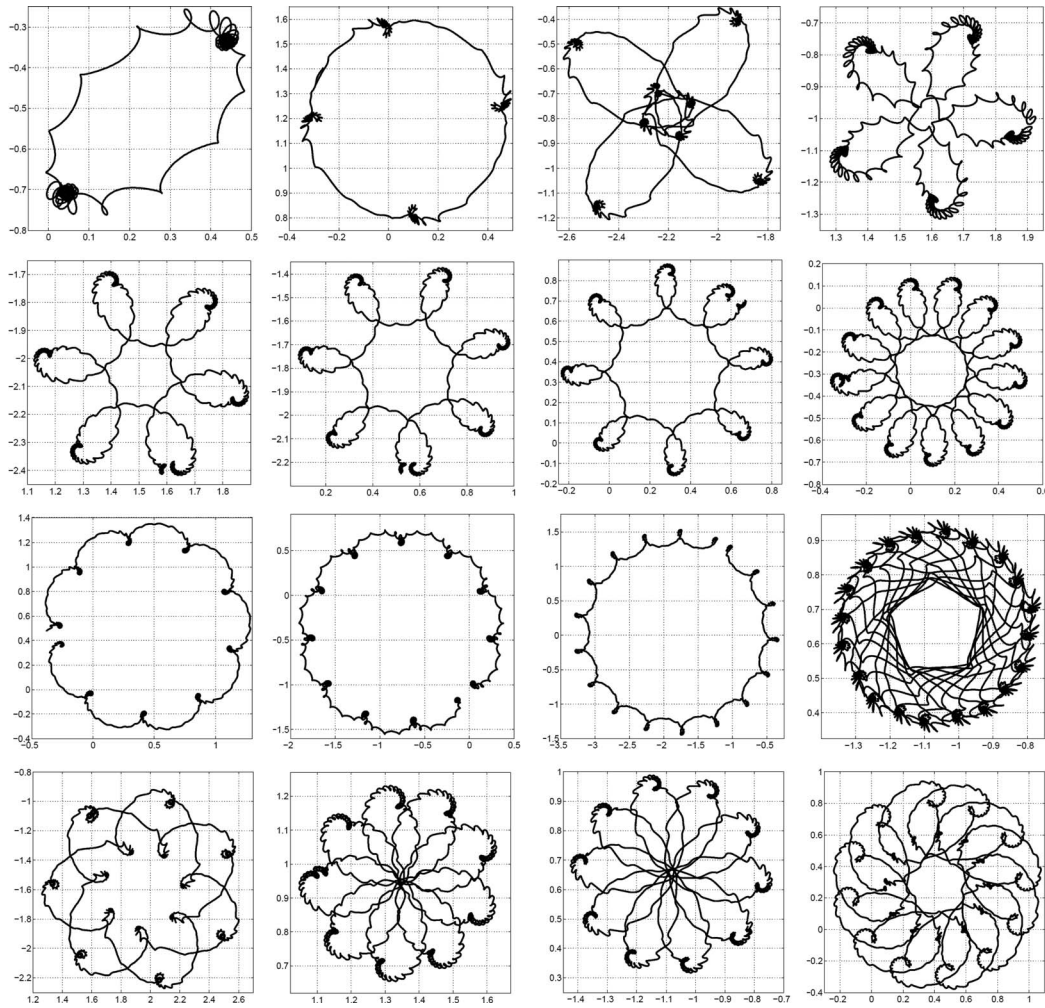


FIG. 9. Numerical simulations of wobble-and-leap trajectories at $n = 0$, for various values of the initial radius r_0/λ_F and vibrational forcing γ/γ_F . The plots show the paths of the orbital centers, nondimensionalized by the Faraday wavelength, $(\bar{x}_c(t), \bar{y}_c(t))/\lambda_F$. From top left to bottom right, the parameter values are: $(r_0/\lambda_F, \gamma/\gamma_F) = (0.376, 0.9665), (0.370, 0.966), (0.3769, 0.9665), (0.365, 0.966), (0.3654, 0.966), (0.3657, 0.966), (0.3659, 0.966), (0.3656, 0.966), (0.368, 0.966), (0.373, 0.9665), (0.372, 0.9665), (0.3763, 0.9665), (0.3775, 0.9665), (0.3647, 0.966), (0.370, 0.9665), and (0.370, 0.967)$.

orbital radius $\bar{r}(t)$ grow (panel (a)). This wobbling phase persists for roughly five orbital periods, before it is interrupted by the rapid shift of the orbital center $\bar{x}_c(t)$ to a new location. The extended trajectory $\mathbf{x}(t)$ is indicated by the dashed gray curve in panel (b), and the orbital center $\bar{x}_c(t)$ by the solid black curve. The walker essentially jumps between various wobbling orbits, which are marked by circles (dashed black curves) centered at the transiently stable orbital centers (black dots). We note that the average leap distance is $(0.342 \pm 0.038)\lambda_F$, quite close to the first zero of $J_0(k_F r)$ at $0.383\lambda_F$, which roughly corresponds to the radius of a circular orbit at $n = 0$. A similar phenomenon was observed in the experiments of Harris and Bush,¹⁶ who reported a qualitatively similar trajectory (panel (e)).

While we did not find any wobble-and-leap trajectories at $n = 1$ for which the orbital center $\bar{x}_c(t)$ followed a nearly periodic path, many were found at $n = 0$. Several such trajectories are shown in Fig. 9, which were found by varying the initial orbital radius r_0 and forcing acceleration γ/γ_F over the narrow parameter range denoted by the purple portion of the $n = 0$ region in Fig. 2. The figure shows the orbital centers $\bar{x}_c(t)$, the darker portions denoting the transiently stable orbital centers. Such trajectories are characterized by an extended wobbling phase which typically lasts more than 20 orbital periods. As is evident from Fig. 2, circular orbits generally destabilize into

wobble-and-leap trajectories for $n = 0$, rather than into wobbling orbits as they do for $n = 1$ and $n = 2$.

VI. OTHER PERIODIC AND QUASIPERIODIC ORBITS

As the memory is increased progressively, the walker's trajectory becomes more complex. An assortment of other periodic or quasiperiodic trajectories is shown in Fig. 10. These trajectories, colored light blue in Fig. 2, have not yet been observed in laboratory experiments, presumably because they arise in such a limited region of parameter space. Many of them represent periodic windows in an otherwise chaotic regime.

A closer look at the trajectory shown in Fig. 11(a) reveals that it may be decomposed into the repeated loop shown in Fig. 11(b), which traverses a larger circle. The loop itself can be viewed as a combination of a larger loop (solid curve) and smaller loop (dashed curve). To quantify this, the loop radius $R(t)$ of the trajectory was computed using a modified osculating circle method with angle $\alpha = \pi/2$, which is described in the Appendix of Harris and Bush.¹⁶ The time trace of $R(t)$ is shown in Fig. 11(c), the gray portion corresponding to the loop in panel (b). It is evident that the loop radius executes persistent periodic oscillations between levels.

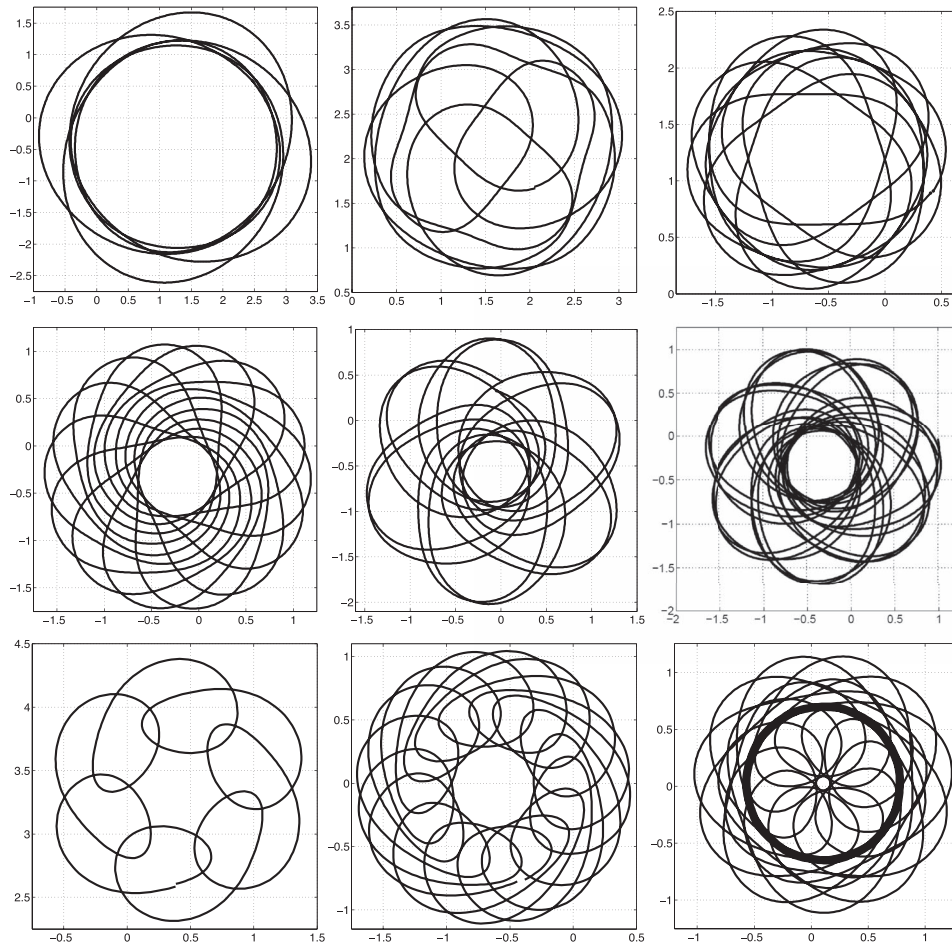


FIG. 10. Numerical simulations of quasiperiodic trajectories observed for various values of the initial orbital radius r_0/λ_F and vibrational forcing γ/γ_F . The plots show the trajectories nondimensionalized by the Faraday wavelength, $(x(t), y(t))/\lambda_F$. From top left to bottom right, the parameter values are: $(r_0/\lambda_F, \gamma/\gamma_F) = (1.4007, 0.97)$, $(0.8924, 0.969)$, $(0.8898, 0.966)$, $(0.8778, 0.966)$, $(0.8398, 0.961)$, $(0.8249, 0.960)$, $(0.3897, 0.976)$, $(1.2348, 0.979)$, and $(0.8417, 0.969)$.

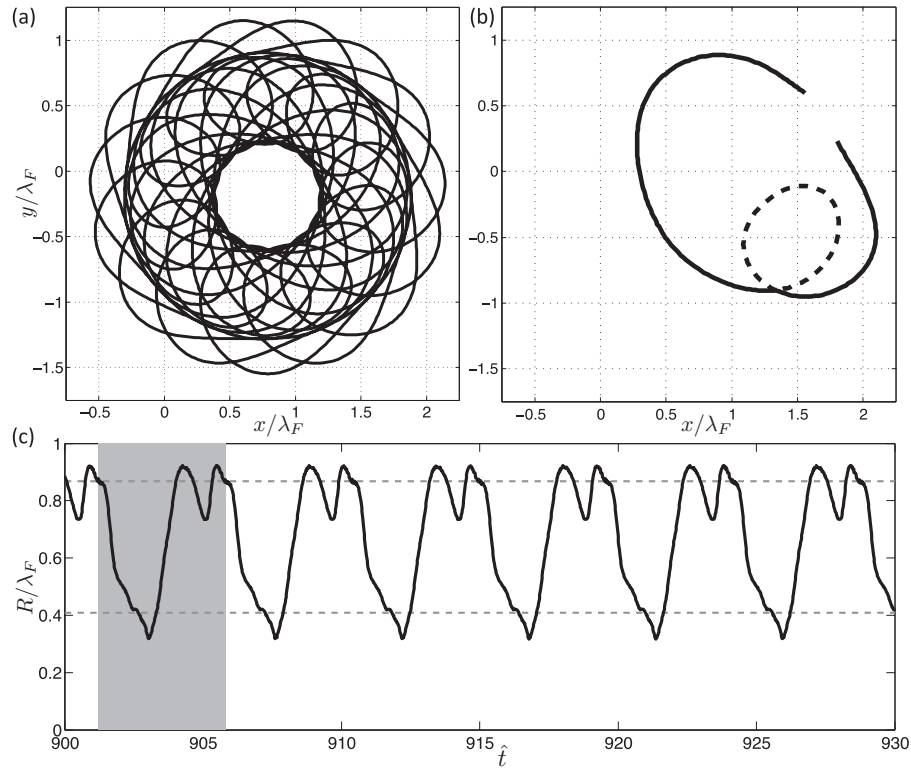


FIG. 11. Numerical simulation of a trajectory exhibiting a periodic oscillation between two orbital radii, obtained using initial radius $r_0/\lambda_F = 1.2691$ and vibrational forcing $\gamma/\gamma_F = 0.971$. Panel (a) shows the trajectory, which consists of the loop in panel (b) drifting along a circle. Panel (c) shows the loop radius $R(t)$ of the trajectory. The shaded portion corresponds to the trajectory in panel (b). The walker evidently oscillates periodically between the two unstable orbital solutions with radii $r_0/\lambda_F = 0.409$ and $r_0/\lambda_F = 0.869$, indicated by the horizontal lines.

To elucidate the origin of this dynamics, we note that a number of unstable circular orbit solutions exist at this value of Ω and γ/γ_F , two of which have the radii indicated by the horizontal lines in Fig. 11(c). The complex trajectory in panel (a) appears to result from the walker jumping periodically between these unstable solutions. Based on the analogy between the Coriolis force on a walker and Lorentz force on an electron,⁴ we note that this trajectory is reminiscent of a Rabi oscillation, a quantum mechanical phenomenon in which an electron periodically jumps between two energy states in the presence of an oscillating magnetic field.²¹ The possibility of forcing such an oscillation in this pilot-wave system by varying the rotation rate Ω will be pursued elsewhere.

VII. CHAOTIC PILOT-WAVE DYNAMICS

As the forcing acceleration γ approaches the Faraday instability threshold γ_F , the trajectories become increasingly complex and chaotic, as indicated by the yellow regions in Fig. 2. An example of such a trajectory is shown in Fig. 12(a). To analyze such a complex trajectory, we compute its local loop radius $R(t)$ using a modified osculating circle method¹⁶ with angle $\alpha = \pi/2$. The time trace of the loop radius is shown in panel (b), and the corresponding histogram in panel (c). The zeros of the Bessel function $J_0(k_F r)$, indicated by the dashed vertical lines, approximate well the maxima of the histogram, indicating that the chaotically evolving walker prefers to make loops roughly quantized on half the Faraday wavelength. It was previously shown¹⁷ that, in the high-memory regime, $\gamma/\gamma_F \rightarrow 1$, the orbital radii defined by (4) may be approximated by the zeros of $J_0(k_F r)$ and $J_1(k_F r)$. While all such orbital solutions are unstable, the former are less unstable than the latter,¹⁸ as indicated by the eigenvalues of the linear stability problem. The footprint of these unstable circular orbits is thus

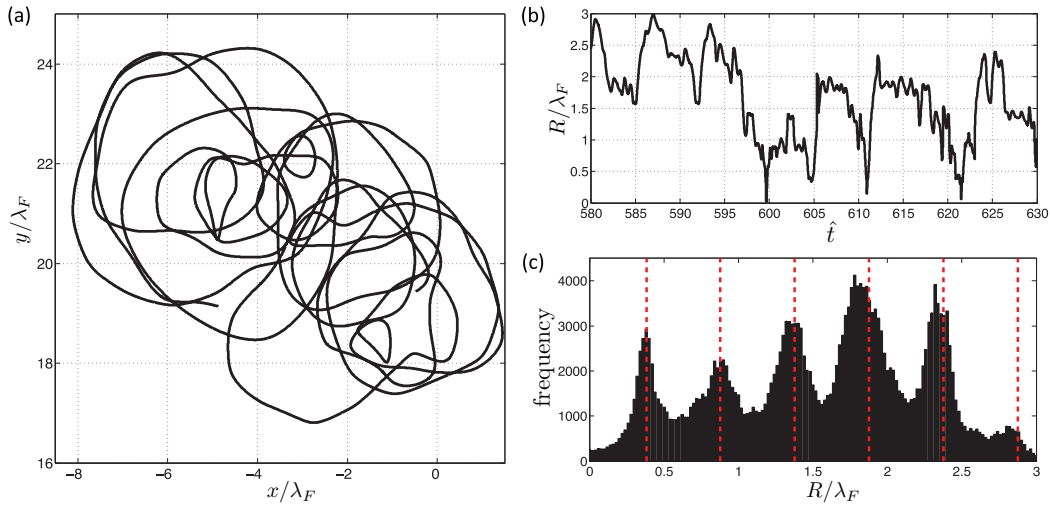


FIG. 12. Numerical simulation of a chaotic trajectory in the high-memory regime, using time step $\Delta t = 2^{-8}$ and $t_{max} = 1000$. Panel (a) shows a portion of the trajectory, obtained using initial orbital radius $r_0/\lambda_F = 2.3775$ and vibrational forcing $\gamma/\gamma_F = 0.985$. Panel (b) shows the corresponding loop radius $R(t)$ over the same time interval, and panel (c) the histogram of the loop radius over the entire trajectory. The bin size is fixed at $0.02\lambda_F$. The vertical lines are located at the zeros of the Bessel function $J_0(k_F r)$.

present in the multimodal statistics of the walker's loop radius $R(t)$, an effect demonstrated in the laboratory experiments of Harris and Bush.¹⁶

The walker's precise statistical behavior depends on the memory and rotation rate, as shown in Figs. 13 and 14. The top panels in Fig. 13 show the dependence of the statistics of $R(t)$ on the rotation rate Ω for three different values of forcing acceleration γ/γ_F . The vertical slices of the plots at $2\Omega\lambda_F/u_0 \approx 0.5$ correspond to the histograms in the lower panels, the color indicating the frequency count of a particular loop radius. Note that, for fixed forcing acceleration γ/γ_F , increasing the rotation rate shifts the histogram towards smaller loop radii, as expected.

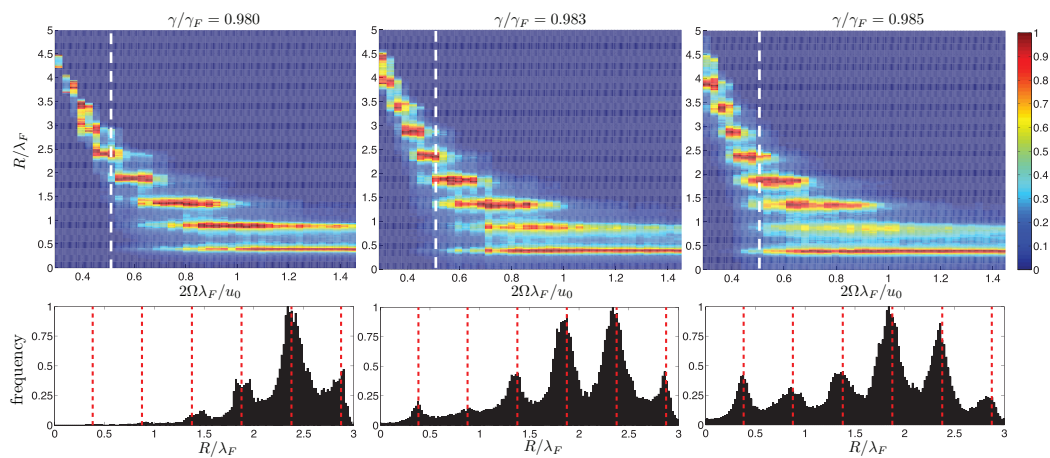


FIG. 13. Numerical simulations showing the dependence of the orbital statistics on the dimensionless rotation rate $2\Omega\lambda_F/u_0$, for three different values of the vibrational forcing γ/γ_F . Each simulation was performed from stationary initial conditions, using time step $\Delta t = 2^{-8}$ and $t_{max} = 1000$. In the top panels, each column is colored according to the prevalence of the corresponding loop radius $R(t)$, with red segments being the most prevalent radii. The bottom panels show three histograms corresponding to $\Omega = 0.17$ (or $2\Omega\lambda_F/u_0 \approx 0.5$), indicated by the vertical lines in the top panels. The peaks of the histograms are centered at the zeros of the Bessel function $J_0(k_F r)$, indicated by the vertical lines. The bin size is fixed at $0.02\lambda_F$.

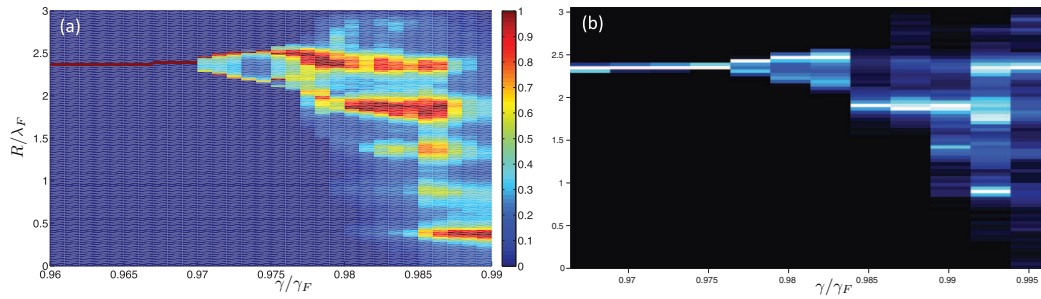


FIG. 14. Numerical simulations showing the dependence of the orbital statistics on the vibrational forcing γ/γ_F . The simulations were initiated with the circular orbit at $n = 4$ corresponding to the fixed dimensionless rotation rate $\hat{\Omega} = 0.1784$ (or $\Omega = 0.70 \text{ s}^{-1}$), with time step $\Delta t = 2^{-8}$ and $t_{\max} = 1000$. In panel (a), each column is colored according to the prevalence of the corresponding loop radius $R(t)$, with red segments being the most prevalent radii. Note that the brightest segments lie near the zeros of $J_0(k_{FR})$. Panel (b) shows the corresponding experimental data from Harris and Bush,¹⁶ obtained for $\Omega = 0.79 \text{ s}^{-1}$.

Figure 14 shows the dependence of the walker statistics on the memory, for a fixed value of the rotation rate. For a given value of γ/γ_F , the simulations were initiated with the circular orbit at $n = 4$. As in Fig. 13, each vertical column of Fig. 14(a) represents a histogram of $R(t)$. At low values of memory, a single circular orbit solution is accessible, as is indicated by the horizontal line. As the memory is progressively increased ($\gamma/\gamma_F \geq 0.97$), more orbital solutions become accessible. The orbital solutions then destabilize into wobbling orbits, then chaotic trajectories, as indicated by the broadening of the histograms. While all of the orbital solutions are unstable at high memory,¹⁸ the sharp red bands in Fig. 14(a) reflect their persistent influence on the walker statistics.

VIII. DISCUSSION

We have numerically simulated an integro-differential trajectory equation for the horizontal motion of a walker in a rotating frame. The results may be summarized in a regime diagram (Fig. 2), which delineates the dependence of the walker's trajectory on system parameters. Our numerical results rationalize the destabilization of circular orbits into wobbling orbits, drifting orbits, and wobble-and-leap orbits, all of which were found in the laboratory experiments of Harris and Bush.¹⁶ Indeed, many of these exotic trajectories were predicted by the numerical simulations and subsequently observed experimentally.

For 2ω -wobbling orbits, the wobbling amplitudes and frequencies obtained in the numerical simulations are consistent with those reported in experiments.¹⁶ Our simulations predict the existence of 3ω -wobbling orbits, which are expected to arise in a small region of parameter space. We have demonstrated that drifting orbits arise from the instability of 2ω -wobbling orbits. The orbital centers of drifting and wobble-and-leap orbits traverse a variety of periodic and quasiperiodic paths, revealing a rich nonlinear dynamics whose form depends strongly on both the bath rotation rate Ω and vibrational forcing γ/γ_F .

While the walker's trajectory becomes chaotic in the high-memory limit, $\gamma/\gamma_F \rightarrow 1$, its loop radius has a multimodal statistical behavior with peaks at the zeros of the Bessel function $J_0(k_{FR})$, an effect observed in the experiments of Harris and Bush.¹⁶ In this regime, the radii of circular orbits may be approximated¹⁷ by the zeros of $J_0(k_{FR})$ and $J_1(k_{FR})$. Linear stability analysis shows that these solutions are unstable, the former being less unstable than the latter.¹⁸ The walker thus jumps intermittently between the least unstable orbital solutions, whose influence is apparent in the coherent multimodal statistics. A similar behavior has recently been observed by Couder *et al.*,²³ who report that the complex motion of a walker in a harmonic potential may be characterized by intermittent transitions between a set of quasiperiodic orbits.

The relatively small discrepancies between the laboratory experiments of Harris and Bush¹⁶ and the numerical results reported herein most likely arise from our neglect of the walker's vertical dynamics, as the trajectory equation (2) is obtained by time-averaging the forces on the walker

over the bouncing period. We also assume the phase $\sin \Phi$ to be constant, while it is known to depend weakly on the vibrational forcing γ/γ_F and fluid viscosity.¹¹ Nevertheless, the satisfactory agreement between the experiments and model predictions suggests that the essential features of the walker's pilot-wave dynamics are captured by the trajectory equation (2).

In their study of walker dynamics in a harmonic potential, Perrard *et al.*²² also report complex orbits, including lemniscates and trefoils centered at the origin. They interpret these complex orbits in terms of a double quantization in mean radius and angular momentum of the observed trajectories. In our system, while quantization of the angular momentum in the circular orbits was clearly evident, no such double-quantization was apparent. Specifically, we find that the mean radius and angular momentum of drifting orbits depends continuously rather than discretely on the rotation rate Ω , as suggested by Fig. 6. We note, however, that the walker dynamics in these two systems is qualitatively different, as the orbital center is not imposed in the rotating system. While we observe erratic trajectories at high memory, one can imagine that quantized drifting orbits might arise for a different choice of fluid parameters, or in a more general pilot-wave setting.

Having benchmarked our model against the experimental results of Harris and Bush,¹⁶ we may now turn our attention to pilot-wave systems with different external forces and geometries. In future work, we plan to numerically characterize the dynamics of a walker in a harmonic potential, a system currently being studied experimentally and numerically by the Paris group.²² A similar approach will also enable us to study pilot-wave systems that are not accessible in the laboratory. It is our hope that such an investigation into the rich nonlinear pilot-wave dynamics of walkers will yield further insight into their quantum-like behavior.

ACKNOWLEDGMENTS

The authors gratefully acknowledge the generous financial support of the NSF through Grant Nos. CBET-0966452 and CMMI-1333242, and R.R.R. partial support through Grant Nos. DMS-1007967, DMS-1115278, and DMS-1318942. A.U.O. and D.M.H. also acknowledge support through the NSF Graduate Research Fellowship Program, and A.U.O. that of the Hertz Foundation. Ø.W.-W thanks the Danish National Advanced Technology Foundation for support through the NanoPlast project. The authors also thank Yves Couder and Emmanuel Fort for valuable discussions.

- ¹ J. W. M. Bush, "Quantum mechanics writ large" *Proc. Natl. Acad. Sci. U.S.A.* **107**(41), 17455–17456 (2010).
- ² Y. Couder and E. Fort, "Single-particle diffraction and interference at a macroscopic scale" *Phys. Rev. Lett.* **97**, 154101 (2006).
- ³ A. Eddi, E. Fort, F. Moisy, and Y. Couder, "Unpredictable tunneling of a classical wave-particle association" *Phys. Rev. Lett.* **102**, 240401 (2009).
- ⁴ E. Fort, A. Eddi, A. Boudaoud, J. Moukhtar, and Y. Couder, "Path-memory induced quantization of classical orbits" *Proc. Natl. Acad. Sci. U.S.A.* **107**(41), 17515–17520 (2010).
- ⁵ A. Eddi, J. Moukhtar, S. Perrard, E. Fort, and Y. Couder, "Level splitting at macroscopic scale" *Phys. Rev. Lett.* **108**, 264503 (2012).
- ⁶ D. M. Harris, J. Moukhtar, E. Fort, Y. Couder, and J. W. M. Bush, "Wavelike statistics from pilot-wave dynamics in a circular corral" *Phys. Rev. E* **88**, 011001 (2013).
- ⁷ L. de Broglie, *Ondes et mouvements* (Gauthier-Villars, Paris, 1926).
- ⁸ L. de Broglie, "Interpretation of quantum mechanics by the double solution theory" *Ann. Fond. Louis de Broglie* **12**, 4 (1987).
- ⁹ M. Faraday, "On a peculiar class of acoustical figures, and on certain forms assumed by groups of particles upon vibrating elastic surfaces" *Philos. Trans. R. Soc. London* **121**, 299–340 (1831).
- ¹⁰ A. Eddi, E. Sultan, J. Moukhtar, E. Fort, M. Rossi, and Y. Couder, "Information stored in Faraday waves: the origin of path memory" *J. Fluid Mech.* **674**, 433–463 (2011).
- ¹¹ J. Moláček and J. W. M. Bush, "Drops walking on a vibrating bath: towards a hydrodynamic pilot-wave theory" *J. Fluid Mech.* **727**, 612–647 (2013).
- ¹² S. Protière, A. Boudaoud, and Y. Couder, "Particle-wave association on a fluid interface" *J. Fluid Mech.* **554**, 85–108 (2006).
- ¹³ J. Moláček and J. W. M. Bush, "Drops bouncing on a vibrating bath" *J. Fluid Mech.* **727**, 582–611 (2013).
- ¹⁴ Ø. Wind-Willassen, J. Moláček, D. M. Harris, and J. W. M. Bush, "Exotic states of bouncing and walking droplets" *Phys. Fluids* **25**, 082002 (2013).
- ¹⁵ A. U. Oza, R. R. Rosales, and J. W. M. Bush, "A trajectory equation for walking droplets: hydrodynamic pilot-wave theory" *J. Fluid Mech.* **737**, 552–570 (2013).

- ¹⁶D. M. Harris and J. W. M. Bush, “Droplets walking in a rotating frame: from quantized orbits to multimodal statistics” *J. Fluid Mech.* **739**, 444–464 (2014).
- ¹⁷A. U. Oza, D. M. Harris, R. R. Rosales, and J. W. M. Bush, “Pilot-wave dynamics in a rotating frame: on the emergence of orbital quantization” *J. Fluid Mech.* **744**, 404–429 (2014).
- ¹⁸A. U. Oza, “A trajectory equation for walking droplets: hydrodynamic pilot-wave theory,” Ph.D. thesis (Massachusetts Institute of Technology, 2014), Chap. 5.
- ¹⁹K. Kumar, “Linear theory of Faraday instability in viscous fluids” *Proc. R. Soc. A* **452**, 1113–1126 (1996).
- ²⁰J. C. Butcher, *Numerical Methods for Ordinary Differential Equations*, 2nd ed. (John Wiley & Sons, Chichester, 2008).
- ²¹C. Cohen-Tannoudji, B. Diu, and F. Laloë, *Quantum Mechanics* (John Wiley & Sons, 1977).
- ²²S. Perrard, M. Labousse, M. Miskin, E. Fort, and Y. Couder, “Self-organization into quantized eigenstates of a classical wave-driven particle” *Nat. Commun.* **5**, 3219 (2014).
- ²³Y. Couder *et al.*, personal communication (2014).